PCCP

ROYAL SOCIETY OF CHEMISTRY

PAPER

View Article Online
View Journal

Cite this: DOI: 10.1039/d5cp03811a

Disentangling Norrish-type and Rh catalysed decomposition of aldehydes for use as CO donors

Jasmin Hack,[a] Alina Schmitt,[a] Maik Seemann,[a] Daniel Pech,[a] Tianbai Huang[b] and Robert Geitner *[a]

Received 2nd October 2025,
Accepted 1st March 2026

DOI: 10.1039/d5cp03811a

rsc.li/pccp

This study presents a detailed mechanistic investigation of the photocatalytic decomposition of different aldehydes *via* various Norrish reaction pathways and their subsequent role in the carbonylation of hydrocarbons, particularly toluene, using [Rh(PMe$_3$)$_2$(Cl)(CO)] as a catalyst. Utilizing ^{1}H NMR spectroscopy, we quantitatively analysed the kinetics of the reaction network, focusing on the formation of key products such as alkanes and alkenes. The results reveal multiple well-explainable structure–property relationships for different aldehyde structures. In addition, the presence of [Rh(PMe$_3$)$_2$(Cl)(CO)] significantly suppresses the decomposition rates, suggesting intersystem crossing between photoactivated aldehydes and the Rh complex, potentially reducing the aldehyde's excited state lifetime. Furthermore, we explored the structural characterization of Rh–phosphine complexes formed during the reaction, though the exact structures remain elusive.

Introduction

Aldehydes exhibit versatile reactivity in organic chemistry and catalysis and are thus valuable building blocks in industry. Notably, the production of aldehydes *via* the hydroformylation of alkenes is one of the main applications of homogeneous catalysis in industry.[1] In a hydroformylation reaction, syngas, which consists of hydrogen and carbon monoxide (CO), in conjugation with a late transition metal catalyst (*e.g.* Pd or Rh), is used to extend the carbon chain of an alkene by one carbon atom while simultaneously adding the desired aldehyde functionality.

Conversely, the carbonyl group can be removed *via* photochemical activation of the aldehyde. This direct activation of carbonyl groups happens *via* the absorption of UV light. In general, the molecule transitions from a singlet to a triplet state from which further reactions can happen. These follow-up reactions were first described in 1932 and are known as Norrish reactions.[2]

Four types of Norrish reactions can be related to aldehyde decarbonylation (see Scheme 1). In a Norrish-type I (NT1) reaction, the C–C bond of the aldehyde (**1**) dissociates homolytically after photoactivation, leading to the formation of a formyl and an alkyl or aryl radical. The formyl radical is further stabilized by CO elimination or by the hydrogen abstraction on the β-carbon. The different stabilization pathways lead to different products: in the first case, a hydrocarbon (**2**) formed by the recombination of the alkyl or aryl radical with the hydrogen atom and the eliminated CO can be found. In the second case, formaldehyde and an alkene (**3**), which is formed by the intramolecular recombination following β-hydrogen abstraction, can be identified.

The third reaction pathway is the Norrish-type II (NT2) reaction in which the activated aldehyde abstracts a hydrogen atom in the γ-position. The biradical is stabilized by α–β-scission, leading to the formation of a terminal alkene and an enol. The enol subsequently tautomerizes into an aldehyde (**4**). If the α–β C–C bond was initially not part of a ring system, a separate acetaldehyde molecule is formed. The fourth and final pathway is the Norrish–Yang reaction, which leads to the formation of a cyclobutene derivative.[3]

In addition to Norrish-type (NT) decompositions, transition metal complexes, especially Ir, Ru, and Rh, are known to catalyse the decarbonylation of aldehydes, acyl halides, aroyl halides, and ketones.[4] For aldehydes, decarbonylation may happen above 200 °C when [Rh(Cl)(PPh$_3$)$_3$] and [RhCl(CO)(PPh$_3$)$_2$] are used as catalysts.[5] These high temperatures limit the synthetic use of thermal decarbonylation. As first reported by Geoffroy *et al.* in 1976, another possibility is the use of UV light to activate transition metal complexes.[6] Krishnan and Schultz investigated the photolysis of [Rh(Cl)(CO)(PMe$_3$)$_2$] at 308 nm and speculated about the existence of [Rh(Cl)(PMe$_3$)$_2$] after photoactivation.[7] We recently described the system with quantum chemical methods and also found that the loss of CO is a prerequisite for

[a] Technische Universität Ilmenau, Institute of Chemistry and Bioengineering, Group of Physical Chemistry/Catalysis, Weimarer Str. 32, 98693 Ilmenau, Germany. E-mail: robert.geitner@tu-ilmenau.de
[b] Institute for Physical Chemistry (IPC) and Abbe Center of Photonics, Friedrich Schiller University Jena, Helmholtzweg 4, 07743 Jena, Germany

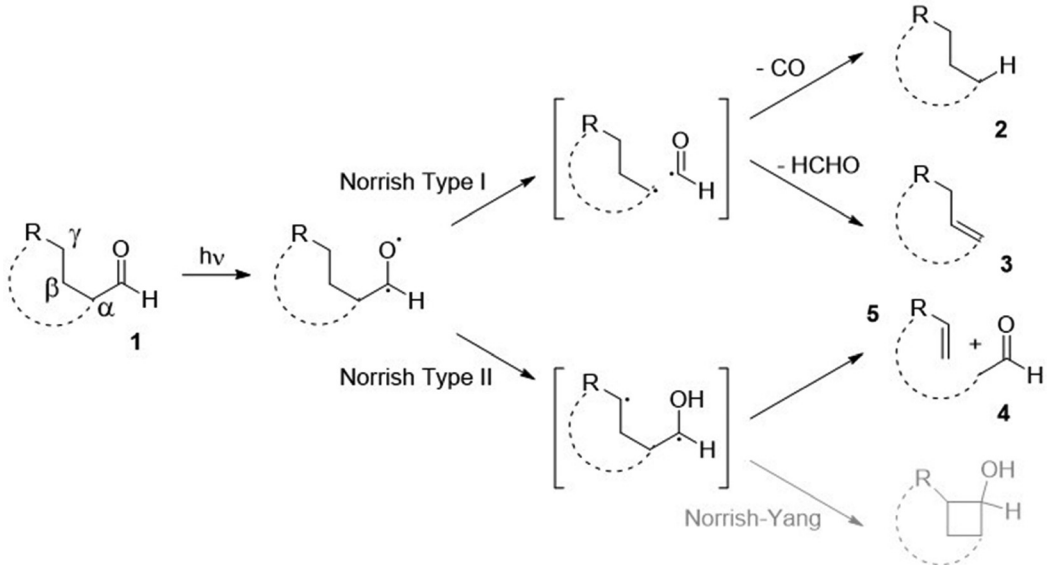

Scheme 1 Summary of different NT reaction pathways after the photoactivation of (cyclic) aldehydes.

subsequent C–H activation.[8] Ford *et al.* investigated complexes of the type $[Rh(Cl)(CO)(PR_3)_2]$ and also found that when the Rh complex is subjected to irradiation with wavelengths larger than 350 nm, the CO ligand dissociates from the complex, which enables further reactions.[9–11] For aldehydes, decarbonylation continues through the C–H activation reaction and decomposition of the acyl fragment before CO and the corresponding hydrocarbon are released.[4]

Eisenberg *et al.* found that Ir and Rh complexes are also able to catalyse the carbonylation of hydrocarbons.[12,13] Kunin and Eisenberg proved that $[Rh(Cl)(CO)(PPh_3)_2]$ enables an equilibrium between benzene and CO on the one side and benzaldehyde on the other side. Grigoryan *et al.* improved the catalytic activity by using a mixture of $[Rh(Cl)(CO)_2]_2$ and PMe_3, which could also carbonylate pentane under a CO atmosphere.[14] The disadvantage is that the equilibrium lies on the side of the hydrocarbon $\left(\Delta G_R^\circ = 7.1 \text{ kJ mol}^{-1}\right)$[12] so that its synthetic value is limited. Tanaka *et al.*,[15] Partridge *et al.*,[16] and Choi and Sakakura[17] among others have studied the Rh system to identify possible intermediates and reaction mechanisms.

Recently, Takaya *et al.* merged NT1 reactions and Rh catalysis to achieve the borylation of aryl ketones.[18] Inspired by this report, we wondered about the photophysical interplay between NT and transition metal catalysed decarbonylation reactions, but, to our surprise, we did not find any reports on the matter. Benzaldehyde features an absorption maximum at 286 nm, while $[Rh(Cl)(CO)(PPh_3)_2]$ absorbs light around 300 and 360 nm.[11] Tanaka *et al.* demonstrated that the NT composition can be suppressed when only light of longer wavelength ($\lambda >$ 325 nm) is used to excite $[Rh(Cl)(CO)(PMe_3)_2]$. Simultaneously, they observed that the catalytic activity of the complex was reduced to one-fifth for the carbonylation of hydrocarbons when only light with longer wavelength is used.

To disentangle the contributions of NT and transition metal catalysed decarbonylation reactions of aldehydes when light of wavelengths 300 and 360 nm is available, we used NMR spectroscopy in conjugation with microkinetic modelling. We used the well-studied catalyst $[Rh(PMe_3)_2(Cl)(CO)]$ for decarbonylation and simultaneously utilized the *in situ* generated CO to carbonylate toluene to also assess the C–H activation kinetics. Finally, we used 2D NMR correlation techniques to study the nature of the active Rh catalyst to link the results to our previous quantum chemical studies.[8]

Experimental section

Materials

Unless otherwise stated, all chemicals were used without further purification. Benzaldehyde (**1a**) and benzophenone were purchased from Grüssing GmbH; acetaldehyde (**1b**), *cis*-4-heptenal (**1d**), cyclohexanecarboxaldehyde (**1e**, CHA), toluene (**10**), trimethylphosphine and $[Rh(\mu\text{-}Cl)(CO)_2]_2$ were bought from Sigma Aldrich; octanal (**1c**) was delivered by S3-Chemicals; sodium was bought from Merck KGaA; and toluene-d_8 was received from Eurisotop.

Toluene and toluene-d_8 were dried over sodium/benzophenone and subsequently distilled. $[Rh(PMe_3)_2(Cl)(CO)]$ was prepared according to the literature.[15]

NMR sample preparation

The respective Rh catalyst (6.4 mg, 20 μmol) was opened under argon gas but weighed under ambient conditions. To minimize exposure, this process was carried out rapidly. The carbon monoxide donating aldehyde (1.4 mmol) was then added and argon gas was introduced into the Schlenk tube before dry toluene (2 mL) was added. To remove the oxygen introduced by the aldehyde, a freeze–pump–thaw process was carried out three times. The prepared sample (500 μl) was transferred to a Young tube and subsequently flushed with argon. As a reference, 100 μl of dry toluene-d_8 was added to the Young tube. Accordingly, the aldehyde concentration within the NMR

tube was 0.56 mol L^{-1}, while the catalyst concentration was 8 mmol L^{-1}. The aldehyde was present at a concentration that was 70 times greater than that of the catalyst.

Three types of blanks were prepared: the first type contained neither a catalyst nor an aldehyde, the second type contained benzaldehyde (**1a**) but no [$Rh(PMe_3)_2(Cl)(CO)$] and the third type contained [$Rh(PMe_3)_2(Cl)(CO)$] but no aldehyde. These blank samples were prepared in the same way as stated above, just leaving out the addition of [$Rh(PMe_3)_2(Cl)(CO)$] and/or benzaldehyde (**1a**), respectively.

NMR spectroscopy and irradiation

Following the preparation of the NMR sample, NMR spectra were recorded using a Bruker Spectrospin 300 spectrometer (Spectrospin AG). The spectrometer is operated using TopSpin 1.3 software (Bruker BioSpin 2005). The spectrometer was locked and shimmed using the deuterium from toluene-d_8. Subsequently, a ^{1}H measurement with 16 FIDs and a ^{31}P measurement with 512 FIDs were conducted. The measurement frequency for ^{1}H measurements was 300.13 MHz. The ^{31}P measurements were conducted with ^{1}H broadband decoupling at a measurement frequency of 120.50 MHz.

Following an initial NMR measurement, the samples were irradiated using a type LQ-HXP 120-UV/150.26D mercury xenon vapour lamp from Leistungselektronik JENA GmbH for different time periods. An optical fibre enabled the sample to be irradiated in a selective manner from a distance of 1.5 cm. After an irradiation period, ^{1}H and ^{31}P spectra were collected as stated above. NMR spectra were recorded after 0, 30, 60, 90, 120, 180, 240, 300, 360, 480, 600, 720 and 1680 min, resulting in 13 measurements for each sample.

Four different light intensities (LI) could be set on the user interface of the Hg/Xe lamp. A SpectraPen mini SM110/UVIS measuring device from Photon System Instruments was employed to characterize the different light intensities. The measurements were recorded at a distance of 16 cm from the optical fibre in a wavelength window of 320–700 nm. The measurement results are summarized in Table 1.

An infrared thermometer manufactured by Matzner Messgeräte München (accuracy ± 2 °C or 2%) was utilised to measure the temperature during irradiation. The temperature of the NMR tube was measured from approximately 5 cm. The optical fibre was positioned at 1.5 cm from the NMR tube. The temperature was measured in triplicate at each of the four light intensities after an equilibration of 5 min.

Table 1 Illumination, photon flux and radiance for the utilized Hg/Xe lamp. In addition, the temperature of the NMR tube after 5 min of equilibration is also reported

Intensity setting (LI)	Illuminance [lx]	Photon flux density [μmol m^{-2} s^{-1}]	Radiance [W m^{-2}]	Temperature NMR tube [°C]
1	5150	80.5	19.8	26.5
2	11 700	189.6	46.1	31.0
3	24 800	388.2	94.7	34.0
4	52 300	825.1	204.7	48.8

16 experiments were carried out using four different aldehydes at four different irradiation intensities. For benzaldehyde (**1a**), an additional seven experiments were performed. In the first series, the light-dependent behaviour of benzaldehyde (**1a**) without the Rh catalyst was studied, while the second series focused on the wavelength-dependency of the benzaldehyde (**1a**) decomposition by blocking UV radiation below 310 nm ($A > 2$, less than 1% transmission) using an 8 mm thick window glass slab in front of the light guiding fibre.

The pure solvent and pure catalyst blanks were irradiated with a photon flux density of 189.60 μmol m^{-2} s^{-1}. Additionally, a sample containing benzaldehyde (**1a**) and the Rh catalyst was heated to 50 °C for 1680 min without any irradiation to exclude thermally triggered side reactions (see Fig. S1 and S2).

To verify the reproducibility of the experiments, the measurements at photon flux densities of 80.50 and 189.60 μmol m^{-2} s^{-1} were repeated two additional times for benzaldehyde (**1a**) with the Rh catalyst.

For selected aldehydes and irradiation times, additional 1D and 2D spectra were measured using a Bruker Ascend™ 500 spectrometer from Bruker Switzerland AG. The spectrometer was controlled using TopSpin 4.3.0 software. Using this NMR spectrometer, ^{1}H measurements were recorded with 16 and 512 FIDs with a measurement frequency of 500.13 MHz. The ^{13}C and ^{31}P measurements were recorded ^{1}H broadband decoupled at measurement frequencies of 125.75 MHz (^{13}C) and 202.45 MHz (^{31}P), respectively. For the ^{13}C measurement, 4096 and 1024 FIDs were recorded (see Fig. S3), while 512 FIDs were accumulated for the ^{31}P spectra. In addition, 2D spectra (HSQC, COSY) analysing the coupling of ^{1}H and ^{13}C or ^{1}H and ^{31}P were recorded for selected samples.

NMR data preprocessing

NMR data preprocessing was adapted from the literature.[19] The entire data analysis process was performed using R (4.4.1).[20] The R packages from the tidyverse family were utilized to organize the data and create the figures.[21] First, the NMR FID was drift-corrected by using 5% of the data points recorded at the end of the acquisition period to calculate a mean value, which was subtracted from all FID values. The kth data point from the FID was multiplied with an exponential apodization function featuring a frequency of $W = 2$ Hz.

$$e^{-\pi \cdot W \cdot k \cdot \Delta t} \quad (1)$$

Subsequently, the FID was zero filled by adding 32 768 zeros to the end of the FID resulting in 65 536 data points, which enables the extraction of all recorded information according to the Nyquist–Shannon sampling theorem.[22] Finally, the complex conjugate of the processed FID was Fourier transformed using a fast Fourier transformation algorithm.[23] The resulting NMR spectra were phase-corrected using the graphical user interface of MestReNova (15.0.1-35756).[24] Finally, the NMR spectra were referenced to the toluene methyl signal (2.17 ppm).

Afterwards, the spectra were normalized to the area of the toluene methyl signal (1.95 to 2.45 ppm). The preprocessed

Table 2 Overview of the respective NMR signals of the relevant substances involved in the reaction Scheme 2

Number	Compound	NMR signals [ppm]
1	Aldehyde	9.53–9.74
2	Hydrocarbon	1.36–1.47
3	NT1 alkene	5.61–5.88
4	Acetaldehyde	9.22–9.32
5	NT2 alkene	5.45–5.68
6	Alcohol	4.25–4.43
7	Ethanol	3.30–3.59
8	Methylbenzaldehyde	9.74–9.94
9	Methylbenzyl alcohol	4.43–4.57
10	Toluene	1.85–2.45

NMR spectra were analysed by integrating the respective signals (see Table 2).

The integral regions were slightly adjusted for each aldehyde to fit the exact signal positions. Eqn (2)–(4) were used to transform the signal areas (A_X) into concentrations (c_X).

$$n_X = \frac{A_X}{p_X} \tag{2}$$

$$X_X = \frac{n_X}{\sum_i n_{X,i}} \tag{3}$$

$$c_X = \frac{X_X \cdot \rho_M}{\sum_i X_{X,i} \cdot M_{X,i}} \tag{4}$$

where n_X is the relative number of molecules, p_X the respective proton count, X_X the molar ratio, ρ_M the density of the reaction mixture and $M_{X,i}$ the molecular mass of the ith species. As an approximation, the density of toluene (0.922 g mL^{-1}) was used as ρ_M. This approximation is justified as toluene makes up most of the samples.

Kinetic fitting

Scheme 2 illustrates the reaction pathways that were directly observed by NMR measurements on the one hand and reaction pathways derived from the literature on the other hand. It was from this that differential eqn (5)–(14) were subsequently deduced in order to describe the kinetics. The reaction pathways for the Norrish reactions have been derived from Norrish and Kirkbride[2] as well as from Yang and Yang.[3] The reaction pathway of **2** has also been described by Doughty and Pignolet.[4] The reduction to an alcohol (**6**) and the formation of methylbenzaldehyde (**8**) and methylbenzyl alcohol (**9**) were described in the study by Tanaka *et al.*[15] The R packages FME and deSolve were used to solve the kinetic differential eqn (5)–(14).[25] To fit the rate constants k_1–k_9 to the experimentally determined concentrations, a cost function was defined aiming to minimize the squared sum of residuals. For optimization, the algorithm from Nelder and Mead[26] was used with a lower bound of 0 for the kinetic rate constants. The concentration of toluene was assumed to be constant at 9.41 mol L^{-1}, which corresponds to its concentration in pure toluene. Furthermore, all concentrations smaller than the limit of detection (0.01 mol L^{-1}, three times the standard deviation of the noise recorded between 12 and 14 ppm) were set to 0 for the fitting as we found that the fitting procedure became unstable due to the significant noise contribution from small signals.

$$\frac{d[\mathbf{1}]}{dt} = -k_1[\mathbf{1}] - k_2[\mathbf{1}] - k_3[\mathbf{1}] - k_5[\mathbf{1}] \tag{5}$$

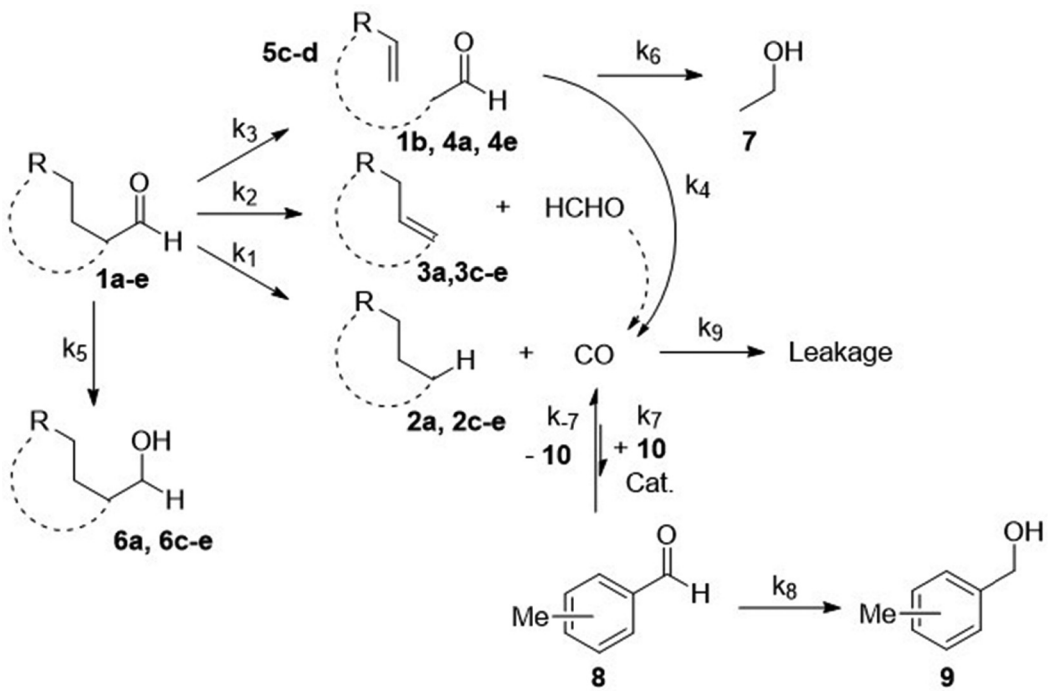

Scheme 2 Possible reaction pathways in the NT decarbonylation of aldehydes (**1a–e**) and the subsequent C–H carbonylation of toluene (**10**).

$$\frac{d[\mathbf{4}]}{dt} = +k_3[\mathbf{1}] - k_4[\mathbf{4}] - k_6[\mathbf{4}] \quad (6)$$

$$\frac{d[\mathbf{2}]}{dt} = +k_1[\mathbf{1}] \quad (7)$$

$$\frac{d[\mathbf{3}]}{dt} = +k_2[\mathbf{1}] \quad (8)$$

$$\frac{d[\mathbf{5}]}{dt} = +k_3[\mathbf{1}] \quad (9)$$

$$\frac{d[\mathrm{CO}]}{dt} = +k_1[\mathbf{1}] + k_2[\mathbf{1}] + k_4[\mathbf{4}] - k_9[\mathrm{CO}] - k_7[\mathrm{CO}][\mathbf{10}] + k_{-7}[\mathbf{8}] \quad (10)$$

$$\frac{d[\mathbf{8}]}{dt} = +k_7[\mathrm{CO}][\mathbf{10}] - k_{-7}[\mathbf{8}] - k_8[\mathbf{8}] \quad (11)$$

$$\frac{d[\mathbf{6}]}{dt} = +k_5[\mathbf{1}] \quad (12)$$

$$\frac{d[\mathbf{7}]}{dt} = +k_6[\mathbf{4}] \quad (13)$$

$$\frac{d[\mathbf{9}]}{dt} = +k_8[\mathbf{8}] \quad (14)$$

An illustration of the reaction network can be seen in Scheme 2 and the results of the fitting procedure can be seen in Table S1 and Fig. S4–S36. When the aldehyde was acetaldehyde (**1b**), a simplified model leaving out eqn (5), (7)–(9) and (12) was used as acetaldehyde can only undergo NT1 decomposition and reduction as only α-hydrogens are available.

UV/Vis spectroscopy

The preparation was carried out under an argon atmosphere at room temperature using standard Schlenk techniques. Dry toluene was added into a handmade Schlenk quartz cuvette, the pressure was equalized, and the weight was determined. This procedure was repeated after the addition of the respective aldehyde or the Rh complex [Rh(PMe$_3$)$_2$(Cl)(CO)].

UV/Vis measurements were performed using a Jasco V-570 spectrometer at a scan rate of 400 scans per min over a wavelength range from 1100 to 200 nm at room temperature (see Fig. S38–S44). Background correction and reference measurements were conducted using a separate cuvette containing toluene. The extinction coefficient ε was determined using Beer's law.

Table 3 Extinction coefficients ε and the respective wavelength positions with the most intense absorption λ_{max} for different aldehydes (**1a–e**)

	Compound	λ_{max} [nm]	ε [L mol^{-1} cm^{-1}]
1a	Benzaldehyde	286	1343.0
1b	Acetaldehyde	284	50.7
1c	Octanal	284	24.3
1d	*cis*-4-Heptenal	284	32.3
1e	Cyclohexanecarboxaldehyde (CHA)	294	32.3

Table 3 summarizes the extinction coefficients ε and the respective wavelength positions with the most intense absorption λ_{max}.

Quantum chemical calculations

All calculations were carried out with the Gaussian 16 software package.[27] Closed-shell equilibrium ground state structures were obtained at the density functional level of theory (DFT) with the B3LYP functional,[28] incorporating the D3BJ dispersion correction.[29] The solvent effect due to benzene was taken into account by employing the solute electron density (SMD) variant of the integral equation formalism of the polarizable continuum model (IEFPCM).[30] A subsequent vibrational analysis was carried out for every optimized structure to verify that a minimum on the 3N-6-dimensional potential energy (hyper)surface (PES) was achieved. The def2-SVP basis set and the corresponding effective core potential (ECP) were utilized for all atoms during structural optimization.[31] The shielding constants for P and H atoms were calculated using the gauge-independent atomic orbital (GIAO) method[32] with the PBE0 functional[33] and 6-311g(2d,2p) basis set.[34] The final ^{31}P shifts were scaled by dividing by a factor of 1.073.[35] The revTPSS functional[36] was utilized for the Rh–P coupling calculations. To account for the effects of the core electrons of the Rh atom, the full-electron jorge-DZP-DKH basis set[37] was employed, while the pcSseg-1 basis set[38] was used for the other atoms.

Results and discussion

Qualitative NMR analysis

Fig. 1 shows an exemplary series of ^{1}H NMR spectra recorded for the decomposition of benzaldehyde (**1a**). The assignments and observations discussed in the following are of a general nature and thus true for all aldehydes and light intensities studied.

In Fig. 1, it can be seen that, as expected, the benzaldehyde (**1a**) signal at 9.63 ppm decreases with increasing reaction time. Benzaldehyde (**1a**) is able to release CO, which can subsequently act as a substrate in a carbonylation reaction. The carbonylation of toluene (**10**) produces methylbenzaldehyde (**8**), which gives rise to a signal at 9.84 ppm, nearly independent of the substitution pattern and thus we cannot differentiate between the different isomers. Methylbenzaldehyde (**8**) is formed *via* the C–H activation of toluene (**10**), which is possible due to the presence of [Rh(PMe$_3$)$_2$(Cl)(CO)].[15] We and others have previously shown that the C–H activation occurs *via* the photoactivation of [Rh(PMe$_3$)$_2$(Cl)(CO)] and the loss of CO to form the active catalyst [Rh(PMe$_3$)$_2$(Cl)].[8,9,39] It is important to note that methylbenzaldehyde (**8**), as an aldehyde itself, can also undergo decarbonylation, leading to the reformation of toluene (**10**) and carbon monoxide.

Three types of Norrish reactions can be related to the aldehyde decarbonylation and the subsequent CO dissociation in our study (see Scheme 1). In addition, the aldehydes can also

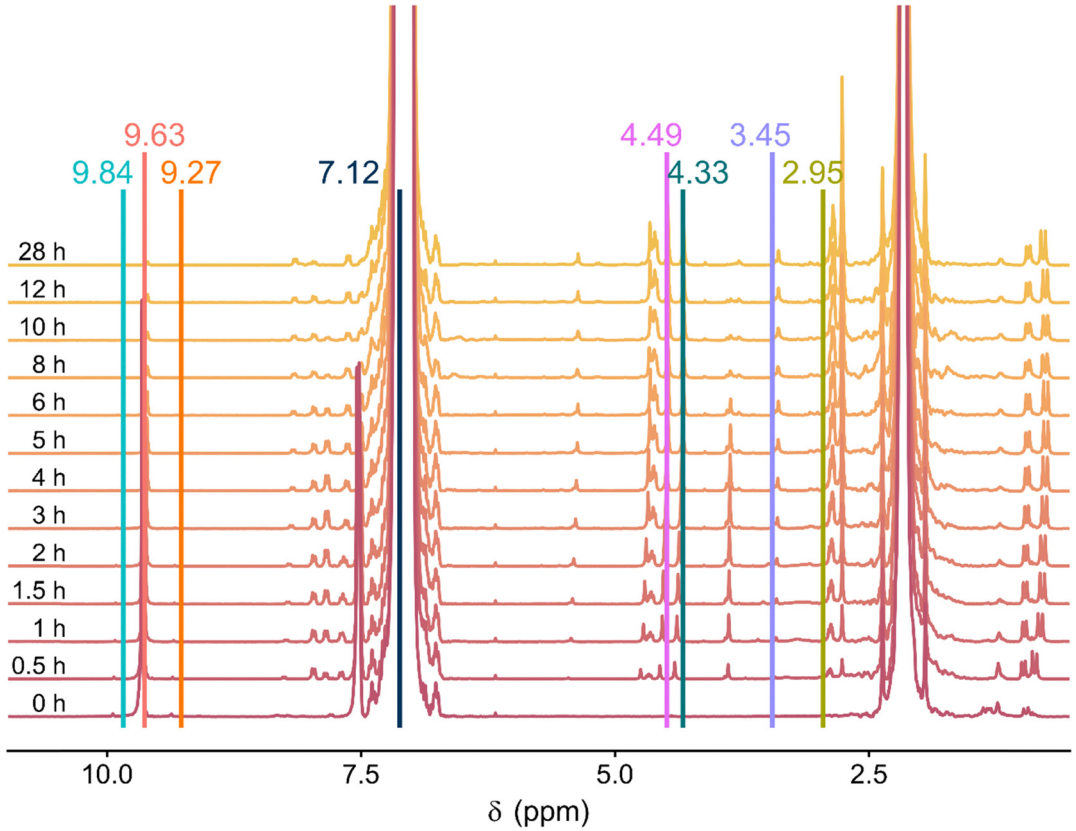

Fig. 1 ^{1}H NMR spectra of the photocatalytic carbonylation of toluene (**10**) using benzaldehyde (**1a**) as the CO source and [Rh(PMe$_3$)$_2$(Cl)(CO)] as the catalyst at a photon flux density of 825.1 μmol m^{-2} s^{-1}. The coloured signal annotations mark the signals which are used for a subsequent kinetic analysis.

undergo metal-catalysed decarbonylation, which is indistinguishable from the NT1 reaction as the products are identical.

At 4.49 and 4.33 ppm, the signals of alcohols – namely benzyl alcohol (**6a**) and methylbenzyl alcohol (**9**) – can be found. These stem from the reduction of the aldehydes **1a** and **8**, respectively, which is an undesired side reaction. The necessary hydrogen stems from the formation of bibenzyl from toluene (**10**). The signal at 2.76 ppm identifies bibenzyl as the coupling product.[40] Interestingly, the integrals from the alcohols and bibenzyl match after normalization to the proton count, hinting that no other reducing agents are involved.

This is in contrast to the results of Tanaka *et al.*, who also found benzophenone and biphenyl as products.[15] Due to the overwhelming intensity of the toluene (**10**) signals, we cannot rule out the formation of methyldiphenylmethanes or dimethylbiphenyls *via* a chain–core or core–core coupling reaction, but looking at the accompanying ^{13}C spectra we can rule out the formation of methyl benzophenone as no new carbonyl group can be observed (see Fig. S3).

In the bigger picture, all three reaction modalities (NT or metal-catalysed decomposition, carbonylation, and reduction) can be summarized in Scheme 2.

When looking at Scheme 2, it becomes obvious that specific aldehydes block certain reaction pathways. For example, the NT2 reaction seems very unlikely when using benzaldehyde (**1a**) as the starting material, as this pathway would break the aromatic system which is energetically unfavourable. The same is true for the NT1 formation of formaldehyde as this would create very reactive benzyne (**3a**). These thoughts can also be verified when looking at the NMR spectra in Fig. 1. As expected, there is no sign of a terminal alkyne group for the NT2 pathway and no sign of benzyne in the ^{13}C spectra (Fig. S3).

The decomposition of smaller aldehydes is also hindered. As no β- or γ-hydrogen is available in acetaldehyde (**1b**), it can only undergo NT1 decomposition, yielding CO and methane (**2b**). For the larger aldehydes studied here, namely octanal (**1c**), 4-*cis*-heptenal (**1d**) and CHA (**1e**), all reaction pathways are available, but not necessarily likely, as the γ-hydrogens in 4-*cis*-heptenal and CHA have limited reactivity, as they are either next to a C=C-double bond or are part of a ring system, respectively.

Kinetic fitting

When combining the qualitative information shown in Scheme 2 with the quantitative information from the NMR spectra, a complete kinetic modelling becomes possible. Fig. 2 illustrates the results of the fitting behaviour, where the rate constants are tuned to match the experimental concentrations. The analogous c–t-diagrams for other aldehydes (**1a–e**) and photon flux densities can be seen in Fig. S5–S36 in the SI.

Fig. 2 exemplarily demonstrates the accuracy of the fitting, thereby validating that the reaction network in Scheme 2

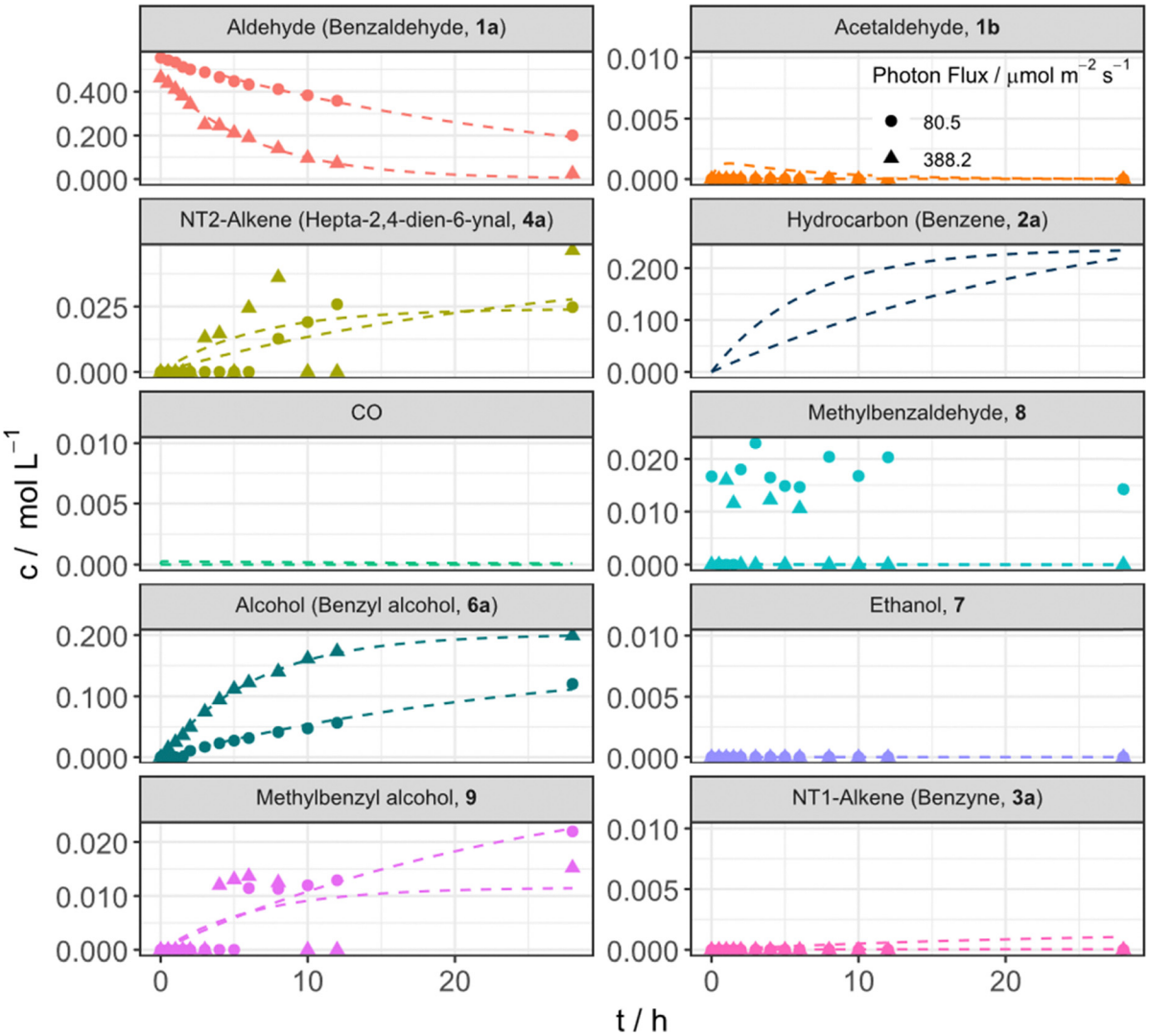

Fig. 2 Experimentally determined concentration for the compounds shown in Scheme 2 and their kinetic fits for the light-driven activation of benzaldehyde (**1a**) and the subsequent carbonylation of toluene (**10**) at photon flux densities of 80.5 (circles) and 388.2 µmol m^{-2} s^{-1} (triangles). For benzene (**2a**) and CO, no experimental concentrations are available and thus only the fitted values derived from the other concentrations are shown.

describes the ongoing reactions properly. As expected, Fig. 2 reveals that benzaldehyde (**1a**) exclusively reacts to form benzene (k_1, **2a**) and benzyl alcohol (k_5, **6a**). The NT2 pathway (k_3) towards **4a** is blocked and no benzyne is formed either (k_2, **3a**). k_1 (2.2×10^{-5} s^{-1}) and k_5 (1.9×10^{-5} s^{-1}) are consequently much larger than k_2 (0 s^{-1}) and k_3 (0.2×10^{-5} s^{-1}) at a photon flux density of 388.2 µmol m^{-2} s^{-1}. Furthermore, Fig. 2 shows that almost no methylbenzaldehyde (**8**) or methylbenzyl alcohol (**9**) is formed. Our explanation for this finding is that the concentration of CO is low due to the slow decomposition of benzaldehyde (**1a**) and that there is a CO leakage from the Young tube (k_9) due to the long reaction and measurement times. This effect is further enhanced by the Eisenberg equilibrium[16,41] in which methylbenzaldehyde (**8**) also decomposes to form CO and toluene (**10**). When looking at the concentration profiles for acetaldehyde (**1b**), a similar trend can be seen (Fig. S5–S8).

The observations change when octanal (**1c**) is used as a starting material. A significant portion of hexene (**5c**) and acetaldehyde (**1b**) can be detected proving that the NT2 reaction took place (k_3 = 0.4×10^{-5} s^{-1} at 388.2 µmol m^{-2} s^{-1}). In contrast to our finding in the liquid phase, Paulson *et al.* found that for heptanal in the gas phase, most of the molecules undergo the NT2 reaction pathway and only a minority follow the NT1 pathway.[42]

For *cis*-4-heptanal (**1d**), the NT2 reaction channel is, as expected, hindered due to the presence of the C=C-bond at the γ-position ($k_3 = 0.1 \times 10^{-5}$ s^{-1} at 388.2 µmol m^{-2} s^{-1}).

Finally, for CHA (**1e**), all possible aldehyde decomposition reactions take place proven by the simultaneous detection of cyclohexane (**2e**), cyclohexene (**3e**), and ω-heptenal (**4e**), which further decomposes into α,ω-pentadien and acetaldehyde (Fig. S21–S25).

It is important to note that, in the conducted experiments, the complex [Rh(PMe$_3$)$_2$(Cl)(CO)] is present as the catalyst to

utilize the *in situ* released CO for carbonylation. A reference experiment with benzaldehyde (**1a**) and without [Rh(PMe$_3$)$_2$(Cl)(CO)] (see Fig. S29–S32) shows four to five times larger reaction rates for the dominant NT1 aldehyde decomposition towards **2a** (k_1 = 6.8 × 10^{-5} s^{-1} at 189.5 μmol m^{-2} s^{-1}).

The added Rh complex is a competitor for light absorption, partly accounting for the decrease of NT decompositions. Nevertheless, due to the low concentration of the Rh complex, the added absorbance cannot fully explain the drastic reduction in the benzaldehyde (**1a**) decomposition rate as one would also expect an increased reaction rate due to the additional metal catalysed decomposition pathway. Therefore, we also speculate that [Rh(PMe$_3$)$_2$(Cl)(CO)] acts as a quencher, leading to the deactivation of aldehyde from the triplet to the singlet ground state. As we have shown in a previous study, [Rh(PMe$_3$)$_2$(Cl)(CO)] and its photoactivated counterparts have multiple close-lying triplet and singlet states, which could facilitate such intersystem crossing.[8] Conversely, the aldehyde can also be viewed as an antenna that promotes the formation of photoactivated Rh complexes, which is necessary for the desired C–H activation process.

When looking at the other different product formations depicted in Scheme 2, only the respective alcohols **6** and methylbenzyl alcohol (**9**) show concentrations above the limit of detection. In cases of larger photon flux densities, methylbenzaldehyde (**8**) can be seen as an intermediate. Although our fitting procedure generates rate constants for these follow-up reactions as well (see Table S1), we refrain from discussing them in detail as the values are subject to significant uncertainty, due to the low concentrations.

Fig. 3 and Fig. S4 depict the rate constants k_1–k_3 and k_5, which contribute to the consumption of various aldehydes (**1a–e**) under different irradiation conditions. Fig. 3a shows the absolute values compared to each other and it becomes clear that for all aldehydes (**1a–e**) the reaction rate increases when the photon flux density is increased. This proves that the reactions are photocatalysed. Furthermore, the two cyclic aldehydes **1a** and **1e** have much larger reaction rates than the three linear aldehydes **1b–d**. The reason for the different reaction rates can be found in their ability to stabilize the respective radicals. After bond fission in the NT1 pathway, a secondary radical is formed in the case of benzaldehyde (**1a**) and CHA (**1e**), while only a primary radical is formed in the case of the three linear aldehydes. Secondary radicals exhibit higher stability than primary radicals thereby increasing their reaction rates.

Fig. 3b shows analysis of the light dependency in detail by normalizing the rate constants with the photon flux density. By doing so, we observe that the rate constants depend nearly linearly on the photon flux density, but with slight deviations from this linearity at larger photon flux densities. The origin of this observation is a saturation effect in which not every new photon from the increased light intensity also leads to a reaction. An outlier can be found for acetaldehyde (**1b**) at a photon flux of 80.5 μmol m^{-2} s^{-1} (LI1) while for the cyclic aldehydes **1a** and **1e**, the NT1 reaction towards the hydrocarbons **2a** and **2e** increases disproportionately. Fig. 3b also indicates that the decomposition rates of different aldehydes vary significantly. This can be explained by the different light absorption behaviours of the aldehydes and quantified by their UV/Vis extinction coefficients ε listed in Table 3. As expected, Table 3 verifies that benzaldehyde (**1a**) has a much higher ε (1343.0 L mol^{-1} cm^{-1} at 286 nm) than the other aldehydes (**1b–e**) in this study due to its aromatic nature and the conjugation with the carbonyl group.

Consequently, Fig. 3c shows the k_1–k_3 and k_5 normalized by the photon flux and the extinction coefficients and reveals that benzaldehyde (**1a**) is the least reactive aldehyde and CHA (**1e**) is the most reactive aldehyde under the same absorption conditions when excluding structural factors. We speculate that this observation can again be attributed to the inhibiting effect of [Rh(PMe$_3$)$_2$(Cl)(CO)]. The structure of benzaldehyde (**1a**) appears to be particularly conducive to facilitate the intersystem crossing in contrast to the aliphatic aldehydes (**1b–e**) in this study. Furthermore, Fig. 3c reveals the influence of the molecular structure on the different reaction pathways while excluding optical effects. Unsurprisingly, *cis*-4-heptenal (**1d**) reacts slower than octanal (**1c**) and avoids the NT2 fragmentation due to the presence of the double bond at the γ position. Octanal (**1c**) is nearly as reactive as *cis*-4-heptenal (**1d**) when looking at the normalized k_1 values, which indicate nearly equal alkane formation. CHA (**1e**) is the most reactive aldehyde as it forms secondary radicals in either case, which increases the reaction rate by a factor of 1.6 when comparing k_1 between CHA (**1e**) and the other three aliphatic aldehydes (**1b–d**).

Finally, Fig. 3d shows the relative ratio of the four rate constants. For acetaldehyde (**1b**) and CHA (**1e**), the reduction towards the alcohol (**6b** and **6e**) decreases at higher photon flux densities while it increases for benzaldehyde (**6a**). The other rate constants are stable in relation to each other under different radiation conditions. This is also expected as k_1–k_3 are linked to the photoactivation of the aldehyde while k_5 is reliant on the availability of a reduction equivalent which is formed *via* the photocoupling of toluene (**10**). It is thus reasonable that the aldehydes (**1a–e**) and toluene (**10**) react differently to the increasing light intensity and that thus also the associated follow-up reactions proceed differently. This is also in line with our previous explanation of the photophysical interaction between the aldehydes **1** and the Rh complex [Rh(PMe$_3$)$_2$(Cl)(CO)] as the complex only influences the light-driven reactions but not the reduction reactions.

Finally, Fig. S4 visualizes the changes when no [Rh(PMe$_3$)$_2$(Cl)(CO)] is present. As discussed, the reaction rates for the benzaldehyde (**1a**) decomposition are higher when the Rh catalyst is not present. An additional control experiment with an 8 mm glass window which absorbs strongly below 310 nm in between the light source and the sample shows that although the NT decomposition is significantly reduced it is not fully stopped either. This makes it impossible to differentiate between the Rh-catalysed and the NT aldehyde decompositions using a simple wavelength cut-off filter.

^{31}P NMR analysis of Rh complexes

With clear observations of C–H activation reactions taking place, we wanted to explore the structure of the involved Rh complexes. A representative ^{1}H–^{31}P HMBC spectrum can be seen in Fig. S37 and the data are summarized in Table 4.

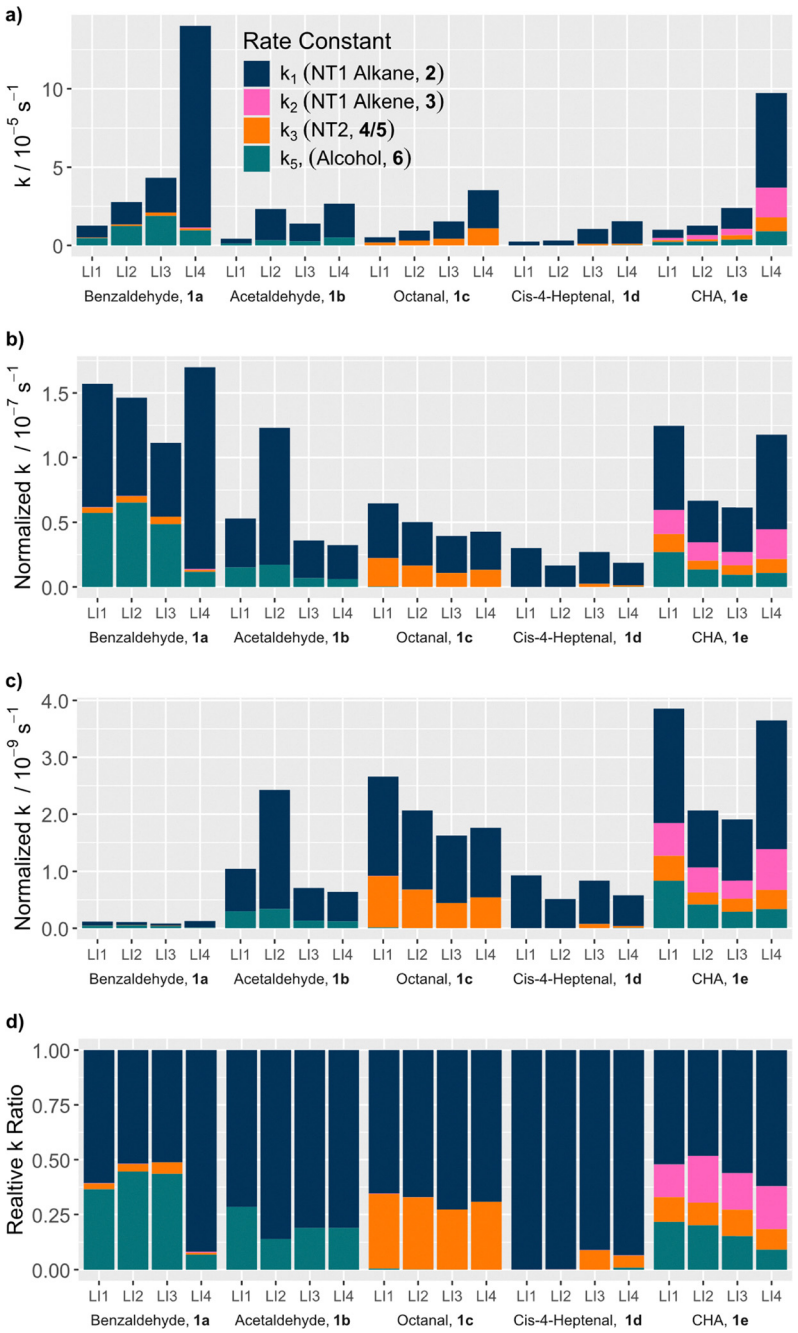

Fig. 3 Rate constants for the light-driven decomposition and reaction of different aldehydes (**1a–e**) depending on the photon flux density (LI, see Table 1 for values). (a) Regular rate constants as extracted by the kinetic fitting procedure. (b) Rate constants normalized by the photon flux density. (c) Rate constants normalized by the photon flux density and the aldehyde extinction coefficient as shown in Table 3. (d) Ratio of the rate constants. The reactions associated with k_1, k_2, k_3, and k_5 can be considered competing reactions.

Ex situ we observe a total of nine correlation signals, each with distinct shifts and coupling constants. All signals appear as doublets in the ^{1}H dimension and eight of them also appear as doublets in the ^{31}P{^{1}H} spectrum. The doublets in the ^{1}H spectra stem from a $^2J_{^1H-^{31}P}$ coupling, while the doublet in the hydrogen decoupled ^{31}P spectra stems from a $^1J_{^{31}P-^{103}Rh}$ coupling for the Rh–phosphine complexes.

The signal at 39.8 ppm can be assigned to trimethyl phosphine oxide Me_3PO. This signal is also visible in the 1D ^{31}P{^{1}H} spectra and is the main deactivation pathway for the Rh catalyst.

By comparing our signals to the ones found by Boyd *et al.*,[16] it is possible to tentatively assign the ^{31}P signals at −9.4 and −7.1 ppm to the complexes **II** and **III** (see Scheme 3),[16] respectively. For the other complexes, we considered multiple structures including [Rh(PMe$_3$)$_3$(CO)]Cl, [Rh(PMe$_3$)$_3$(Cl)],[43] [Rh(μ-Cl)(PMe$_3$)$_2$]$_2$,[43] [Rh(PMe$_3$)$_2$(Cl)(H)(C(O)PhMe)],[44] and *trans*-[Rh(PMe$_3$)$_2$(CO)(Ph)],[16] but none of the

Table 4 $^{1}H-^{31}P$ HMBC data for the reaction of acetaldehyde (**1b**) at a photon flux density of 189.5 μmol m^{-2} s^{-1} after 240 min. For structural information, see Scheme 3

Tentative assignment	$\delta(^{31}P)$/ppm	$\delta(^{1}H)$/ppm	$^{2}J_{^{1}H-^{31}P}$/Hz	$^{1}J_{^{31}P-^{103}Rh}$/Hz
I	−10.2	1.22	7.9	115
II	−9.4	0.96	7	102
III	−7.1	1.03	7.8	103
	−5.5	1.18	9.3	59
	−5.5	0.79	7.5	84
	−4.8	0.85	5.8	122
	−4.8	1.27	8.9	125
	−3.2	1.14	9.5	86
O=PMe_3	39.8	0.96	13.1	—

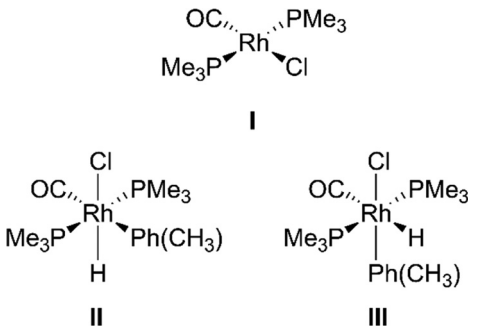

Scheme 3 Rh–phosphine complexes tentatively identified *via* NMR spectroscopy.

existing data fits our ^{31}P shifts nor the observed $^{1}J_{^{31}P-^{103}Rh}$ coupling constants.

To achieve an assignment, we performed density functional theory (DFT) calculations on the ^{31}P shifts as well as the $^{31}P-^{103}Rh$ coupling constants. The results for different Rh–phosphine complexes are summarized in Table S2. To the best of our knowledge, this is the first time that $^{31}P-^{103}Rh$ coupling constants were calculated. While the experimental and DFT calculated shifts are in reasonable agreement, −10.2 compared to −9.7 ppm for $[Rh(PMe_3)_2(Cl)(CO)]$, the values for $^{1}J_{^{31}P-^{103}Rh}$ are further off (115 *vs.* 157 Hz for $[Rh(PMe_3)_2(Cl)(CO)]$). Unfortunately, none of the twelve quantum chemically described structures shown in Table S2, inspired by our previous mechanistic study,[39] matches our experimental observations. We thus have to refrain from final structure assignments at the moment.

Conclusions

In this study, we not only presented a quantitative mechanistic study on the photodecomposition of different aldehydes *via* different Norrish or metal-catalysed reaction pathways but also made a first attempt to disentangle the complex network of different Rh–phosphine complexes that are relevant to the desirable follow-up carbonylation of hydrocarbons. Based on a microkinetic model derived from ^{1}H NMR spectra, it was possible to determine rate constants for the different NT decompositions. Most importantly, this includes the formation of alkanes as well as α- and ω-alkenes. The addition of $[Rh(PMe_3)_2(Cl)(CO)]$ inhibits the photodecomposition disproportionally, which we interpreted as an intersystem crossing between the photoactivated aldehydes and the metal complex.

Our fundamental study sheds light on entangled physicochemical phenomena, which are all relevant when establishing catalytic C–H activation as a tool for the functionalization of hydrocarbons. The knowledge presented here can be applied to establish smaller aldehydes like formaldehyde or acetaldehyde as CO carries in a circular economy.

Author contributions

J. H., A. S. and D. P. performed the NMR sample preparation and NMR measurements. M. S. performed the UV/Vis experiments. R. G. conceptualized the study and performed the kinetic data evaluation. T. H. performed the DFT calculations. J. H., T. H., and R. G. wrote the manuscript and created the figures. All authors reviewed and approved the manuscript.

Conflicts of interest

There are no conflicts to declare.

Data availability

The data (kinetic rate constants for all experiments, additional visualisations of kinetic fits, NMR as well as UV/Vis spectra) supporting this article have been included as part of the supplementary information (SI). The raw spectroscopic data analysed within this study are available from the corresponding author upon request. Supplementary information is available. See DOI: https://doi.org/10.1039/d5cp03811a.

Acknowledgements

The authors would like to thank the Thüringer Aufbaubank (TAB) for funding the 500 MHz NMR spectrometer (2022 FGI 0002). R. G. was funded by the ''Bund-Länder Tenure-Track Program'' of the Federal Ministry of Education and Research (BMBF; FKz.: 16TTP133) as well as by an accompanying grant from the Free State of Thuringia. We gratefully acknowledge funding by the Deutsche Forschungsgemeinschaft (DFG, German Research Foundation, 549144052).

Notes and references

1 R. Franke, D. Selent and A. Börner, *Chem. Rev.*, 2012, **112**, 5675.
2 R. G. W. Norrish and F. W. Kirkbride, *J. Chem. Soc.*, 1932, 1518.
3 N. C. Yang and D.-D. H. Yang, *J. Am. Chem. Soc.*, 1958, **80**, 2913.

4 D. H. Doughty and L. H. Pignolet, in *Homogeneous Catalysis with Metal Phosphine Complexes*, ed. L. H. Pignolet, Springer US, Boston, MA, 1983, pp. 343–375.
5 (*a*) J. Blum, E. Oppenheimer and E. D. Bergmann, *J. Am. Chem. Soc.*, 1967, **89**, 2338; (*b*) J. Tsuji and K. Ohno, *Tetrahedron Lett.*, 1967, **8**, 2173.
6 G. L. Geoffroy, D. A. Denton, M. E. Keeney and R. R. Bucks, *Inorg. Chem.*, 1976, **15**, 2382.
7 R. Krishnan and R. H. Schultz, *Inorg. Chem.*, 2005, **44**, 6691.
8 T. Huang, S. Kupfer, R. Geitner and S. Gräfe, *ChemPhotoChem*, 2024, **8**, e202300219.
9 D. Wink and P. C. Ford, *J. Am. Chem. Soc.*, 1985, **107**, 1794.
10 (*a*) D. A. Wink and P. C. Ford, *J. Am. Chem. Soc.*, 1987, **109**, 436; (*b*) J. S. Bridgewater, B. Lee, S. Bernhard, J. R. Schoonover and P. C. Ford, *Organometallics*, 1997, **16**, 5592.
11 J. S. Bridgewater, T. L. Netzel, J. R. Schoonover, S. M. Massick and P. C. Ford, *Inorg. Chem.*, 2001, **40**, 1466.
12 A. J. Kunin and R. Eisenberg, *J. Am. Chem. Soc.*, 1986, **108**, 535.
13 B. J. Fisher and R. Eisenberg, *Organometallics*, 1983, **2**, 764.
14 N. K. Khannanov, G. N. Menchikova and E. H. Grigoryan, *Mendeleev Commun.*, 1994, **4**, 39.
15 T. Sakakura, T. Sodeyama, K. Sasaki, K. Wada and M. Tanaka, *J. Am. Chem. Soc.*, 1990, **112**, 7221.
16 S. E. Boyd, L. D. Field and M. G. Partridge, *J. Am. Chem. Soc.*, 1994, **116**, 9492.
17 J.-C. Choi and T. Sakakura, *J. Am. Chem. Soc.*, 2003, **125**, 7762.
18 Y. Fujimaki, N. Iwasawa and J. Takaya, *Chem. Sci.*, 2023, **14**, 1960.
19 (*a*) P. Endres, T. Schuett, J. Kimmig, S. Zechel, M. D. Hager, R. Geitner and U. S. Schubert, *Chem. – Eur. J.*, 2023, e202203776; (*b*) P. Endres, T. Schuett, S. Zechel, M. D. Hager, R. Geitner and U. S. Schubert, *RSC Adv.*, 2024, **14**, 14942.
20 R Core team, R: A Language and Environment for Statistical Computing, R Foundation for Statistical Computing, Vienna, Austria.
21 H. Wickham, M. Averick, J. Bryan, W. Chang, L. McGowan, R. François, G. Grolemund, A. Hayes, L. Henry, J. Hester, M. Kuhn, T. Pedersen, E. Miller, S. Bache, K. Müller, J. Ooms, D. Robinson, D. Seidel, V. Spinu, K. Takahashi, D. Vaughan, C. Wilke, K. Woo and H. Yutani, *J. Open Source Software*, 2019, **4**, 1686.
22 (*a*) H. Nyquist, *Trans. Am. Inst. Electr. Eng.*, 1928, **47**, 617; (*b*) V. A. Kotelnikov, Procs. of the first All-Union Conference on the Technological Reconstruction of the Communications Sector and Low-Current Engineering, 1933; (*c*) C. E. Shannon, *Proc. IRE*, 1949, **37**, 10.
23 J. W. Cooley and J. W. Tukey, *Math. Comput.*, 1965, **19**, 297.
24 Mestrelab Research S.L., MestReNova, Mestrelab Research S.L., Santiago de Compostela, Spain.
25 (*a*) K. Soetaert and T. Petzoldt, *J. Stat. Software*, 2010, **33**, 1; (*b*) K. Soetaert, T. Petzoldt and R. Woodrow Setzer, *J. Stat. Software*, 2010, **33**, 1.
26 J. A. Nelder and R. Mead, *Comput. J.*, 1965, **7**, 308.
27 M. J. Frisch, G. W. Trucks, H. B. Schlegel, G. E. Scuseria, M. A. Robb, J. R. Cheeseman, G. Scalmani, V. Barone, G. A. Petersson, H. Nakatsuji, X. Li, M. Caricato, A. V. Marenich, J. Bloino, B. G. Janesko, R. Gomperts, B. Mennucci, H. P. Hratchian, J. V. Ortiz, A. F. Izmaylov, J. L. Sonnenberg, D. Williams-Young, F. Ding, F. Lipparini, F. Egidi, J. Goings, B. Peng, A. Petrone, T. Henderson, D. Ranasinghe, V. G. Zakrzewski, J. Gao, N. Rega, G. Zheng, W. Liang, M. Hada, M. Ehara, K. Toyota, R. Fukuda, J. Hasegawa, M. Ishida, T. Nakajima, Y. Honda, O. Kitao, H. Nakai, T. Vreven, K. Throssell, J. A. Montgomery, Jr., J. E. Peralta, F. Ogliaro, M. J. Bearpark, J. J. Heyd, E. N. Brothers, K. N. Kudin, V. N. Staroverov, T. A. Keith, R. Kobayashi, J. Normand, K. Raghavachari, A. P. Rendell, J. C. Burant, S. S. Iyengar, J. Tomasi, M. Cossi, J. M. Millam, M. Klene, C. Adamo, R. Cammi, J. W. Ochterski, R. L. Martin, K. Morokuma, O. Farkas, J. B. Foresman and D. J. Fox, *Gaussian16 (Revision B.01)*, Gaussian, Inc, Wallingford, CT, USA, 2016.
28 A. D. Becke, *J. Chem. Phys.*, 1993, **98**, 5648.
29 S. Grimme, S. Ehrlich and L. Goerigk, *J. Comput. Chem.*, 2011, **32**, 1456.
30 (*a*) A. V. Marenich, C. J. Cramer and D. G. Truhlar, *J. Phys. Chem. B*, 2009, **113**, 6378; (*b*) B. Mennucci, C. Cappelli, C. A. Guido, R. Cammi and J. Tomasi, *J. Phys. Chem. A*, 2009, **113**, 3009.
31 F. Weigend and R. Ahlrichs, *Phys. Chem. Chem. Phys.*, 2005, **7**, 3297.
32 R. Ditchfield, *Mol. Phys.*, 1974, **27**, 789.
33 C. Adamo and V. Barone, *J. Chem. Phys.*, 1999, **110**, 6158.
34 (*a*) M. M. Francl, W. J. Pietro, W. J. Hehre, J. S. Binkley, M. S. Gordon, D. J. DeFrees and J. A. Pople, *J. Chem. Phys.*, 1982, **77**, 3654; (*b*) R. Krishnan, J. S. Binkley, R. Seeger and J. A. Pople, *J. Chem. Phys.*, 1980, **72**, 650; (*c*) A. D. McLean and G. S. Chandler, *J. Chem. Phys.*, 1980, **72**, 5639.
35 S. K. Latypov, F. M. Polyancev, D. G. Yakhvarov and O. G. Sinyashin, *Phys. Chem. Chem. Phys.*, 2015, **17**, 6976.
36 J. P. Perdew, A. Ruzsinszky, G. I. Csonka, L. A. Constantin and J. Sun, *Phys. Rev. Lett.*, 2009, **103**, 26403.
37 (*a*) B. P. Pritchard, D. Altarawy, B. Didier, T. D. Gibson and T. L. Windus, *J. Chem. Inf. Model.*, 2019, **59**, 4814; (*b*) F. E. Jorge, A. Canal Neto, G. G. Camiletti and S. F. Machado, *J. Chem. Phys.*, 2009, **130**, 64108.
38 F. Jensen, *J. Chem. Theory Comput.*, 2015, **11**, 132.
39 T. Huang, S. Kupfer, M. Richter, S. Gräfe and R. Geitner, *ChemCatChem*, 2022, **14**, e202200854.
40 W. J. Teo, Z. Wang, F. Xue, T. S. Andy Hor and J. Zhao, *Dalton Trans.*, 2016, **45**, 7312.
41 R. Eisenberg, *Isr. J. Chem.*, 2017, **57**, 932.
42 S. E. Paulson, D.-L. Liu, G. E. Orzechowska, L. M. Campos and K. N. Houk, *J. Org. Chem.*, 2006, **71**, 6403.
43 K. Wang, M. E. Goldman, T. J. Emge and A. S. Goldman, *J. Organomet. Chem.*, 1996, **518**, 55.
44 G. P. Rosini, W. T. Boese and A. S. Goldman, *J. Am. Chem. Soc.*, 1994, **116**, 9498.